Surface-Flux Regulation of the Coupling between Cumulus Convection and Baroclinic Waves

WILLIAM J. GUTOWSKI JR. AND WEIDONG JIANG

Department of Geological and Atmospheric Sciences, Iowa State University, Ames, Iowa

(Manuscript received 19 August 1996, in final form 30 July 1997)

ABSTRACT

The authors examine the role of convection in the dynamics of eddy life cycles through numerical experiments using initial states that are baroclinically and conditionally unstable in midlatitudes. The location of wave-induced convection and its influence on the growing wave depends on how strongly the wave is coupled to the lower boundary through surface fluxes. For all three convective schemes used here (Emanuel, modified Grell, modified Kuo), convective destabilization is favored in the wave's warm sector when there are no surface fluxes included in the simulation and in the cold sector when there are. Convection is also shallower when it occurs in the cold sector, though still precipitating. For simulations using Emanuel convection, the relatively shallow convection plays a central role in a water cycle wherein 1) evaporation gives moisture to the cold sector's boundary layer, 2) convection pumps some of the moisture into the lower troposphere above the boundary layer, 3) the large-scale circulation transports the moisture eastward and upward into the wave's warm sector, and 4) stable precipitation condenses the moisture into precipitation. The additional condensation catalyzes a more energetic life cycle by inducing stronger vertical motion and, hence, a greater conversion of available potential energy to kinetic energy. This enhancement, however, is parameterization dependent, with the key factor being how much lower-tropospheric moistening a convection scheme produces.

1. Introduction

The release of latent heat during condensation is an important heating source for the atmosphere. The effect of condensation on the development of midlatitude eddies can be significant and is suggested by early instability analyses and many case studies. A previous study on the life cycles of moist baroclinic eddies (Gutowski et al. 1992, hereafter GBS) helped to delineate the role of moisture condensation in large-scale, nonlinear baroclinic instability. One mechanism of water vapor condensation in the atmosphere is convection. In GBS, convection had a nearly negligible role in the life cycle. However, convection is an important source of heat to the atmosphere, so we have performed further study, focusing on conditions more conducive to the development of convection than the midlatitude climatology used in GBS. As in GBS, we retain a focus on climatological development and the largest amplitude waves in the atmosphere, synoptic and planetary-scale waves, and so we do not stray very far from climatological initial conditions. Thus, our focus is on the relationship between convection and the growing, baroclinic waves that attain largest amplitude in the atmosphere, and not on events such as explosive development or polar cyclones, which tend to be smaller in scale. We also focus on the potential role of eddy moisture transport in fostering convection.

Many case studies have concluded that convective condensation was crucial in the development of the extratropical cyclones examined. Tracton (1973) compared synoptic analyses with numerical forecasts for 21 intense cyclones occurring east of the Rocky Mountains, concluding that cumulus convection played a critical role in initiating development through the release of latent heat in the vicinity of the cyclone center. However, the cases he chose were close to a source of warm moist air, the Gulf of Mexico, thus making them particularly susceptible to the generation of the convective instability and perhaps not representative of general climatological behavior.

Gyakum (1983a,b) analyzed the explosive development of the *QE II* storm of 10–11 September 1978 and hypothesized that a CISK-like mechanism (Charney and Eliassen 1964; Ooyama 1964) operated in which relatively weak baroclinic forcing organized convective heating effects on a scale comparable to the cyclone itself. He further hypothesized that the mechanism may be important to other explosively developing extratropical cyclones. A case study of an extratropical cyclone by Smith et al. (1984) found that convective heating

Corresponding author address: William J. Gutowski Jr., Department of Geological and Atmospheric Sciences, 3021 Agronomy, Iowa State University, Ames, IA 50011-1010.
E-mail: gutowski@iastate.edu.

played a dominant role in forcing cyclone-scale vertical motions during the period of rapid development.

Many analytic studies have also been performed that examine the potential effect of convection on baroclinic instability (e.g., Tokioka 1973; Mak 1982, 1983, 1994; Moorthi and Arakawa 1985; Bannon 1986; Wang and Barcilon 1986; Emanuel et al. 1987; Fantini 1990; Balasubramanian and Yau 1994). Typically, these studies find that convection tends to increase growth rates of the most unstable waves and shift the wavelength of maximum instability toward shorter waves. A common theme in most of these analytic studies is an assumption that the low-level convergence organizes the location and horizontal extent of convection. The degree of low-level convergence in these studies is measured by the large-scale, low-level vertical motion generated by the wave, either by itself or in conjunction with Ekman pumping. In the work of Emanuel et al. (1987) and Fantini (1990), this prescription is modified slightly to a requirement that at each level in the atmosphere, the location of the wave's upward motion determines where moist convective effects modify the large-scale flow.

The results of the study here will suggest that an additional factor for theoretical study to consider is how the wave and associated surface heat fluxes condition the planetary boundary layer as the wave transports warm air and cold air meridionally. An initial indication of this can be seen by comparing the distribution of convection as the wave nears maximum amplitude in two of the life-cycle simulations (Fig. 1), described more completely in later sections. The only difference in the configurations of these two runs is that one includes interaction with the underlying surface (i.e., surface fluxes of heat, moisture, and momentum) and the other does not. Both simulations resemble cases of observed behavior. When surface fluxes are included, convection occurs near the warm front and in the cool air between the warm and cold fronts, similar to behavior observed in case studies by Kuo and Low-Nam (1990) and Kuo et al. (1991). When surface fluxes are not included, much (though not all) of the convection occurs near and ahead of the cold front, similar to behavior observed in case studies by Yau and Jean (1989) and Chang et al. (1996), who also observed substantial convection in the vicinity of the cold front. This difference in behavior provides a further motivation for the life-cycle studies reported here.

We have performed several numerical experiments that are an extension of GBS, focusing on initial states that are conditionally unstable in midlatitudes. A brief description of the model is given in section 2, including upgrades and additions to the version used in GBS. General characteristics of the initial conditions for the life-cycle computations are also described in this section. To aid later discussion, section 3 reviews the vertical temperature structure of growing waves with and without surface heat fluxes present. We then present an analysis of convection during the early (section 4) and mature (section 5) stages of the eddy life cycle. Section 6 gives a discussion and summary of the results.

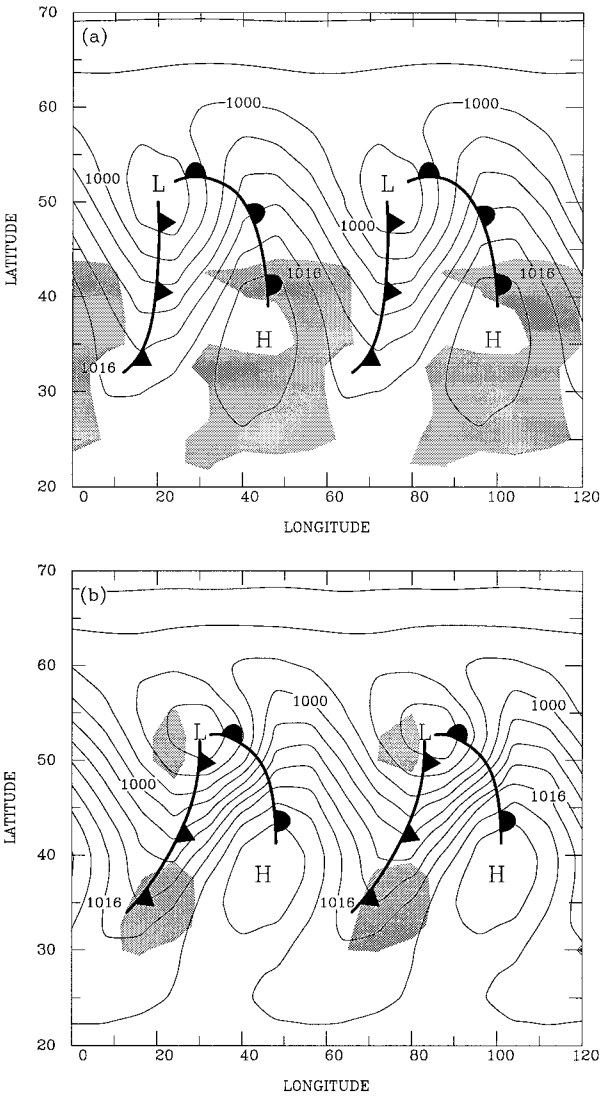

FIG. 1. Distribution of convective heating (shaded area), surface pressure (hPa), and location of fronts as the primary wave in two life-cycle simulations nears maximum amplitude at the end of simulation day 10. The simulations are identical except that (a) includes surface fluxes and (b) does not. Details of the model configuration are described in section 2.

2. Model and initial conditions

The model is a primitive equation, global spectral model (GSM) adapted from the National Centers for Environmental Prediction's GSM, the essence of which is described in Branscome et al. (1989) and GBS. Most features of the model simulations performed by GBS are the same here. Thus model runs include only the zonal average state, a fundamental zonal wavenumber P, and the fundamental wave's next two harmonics (e.g., wavenumbers 0, 7, 14, and 21 for $P = 7$). We assume

symmetry about the equator and resolve latitudinal structure with a spectral truncation in the meridional direction equivalent to rhomboidal 30. The lower boundary is an ocean-covered surface. In this sense the model is more representative of the Southern Hemisphere than the Northern Hemisphere. The surface temperature is equal to the air temperature of the lowest layer of the initial state and does not change throughout the experiment. The latter property is implied by the oceanic lower boundary.

There are two principal differences between the version of the model used by GBS and that used here. First, effects of the planetary boundary layer (PBL) are simulated using parameterizations developed by Troen and Mahrt (1986) in which surface fluxes are represented by similarity theory and turbulent diffusivities above the surface layer are expressed by bulk similarity and matching conditions at the top of the surface layer. To accommodate the upgraded PBL scheme, the model resolves vertical structure using 18 sigma layers, with highest resolution near the surface. Test computations using more and fewer layers show that this resolution is sufficient for our purposes (Jiang 1994). Several layers are also included in the model stratosphere to ensure that an unrealistic wave structure will not develop there that might contaminate tropospheric dynamics.

The other principal difference is the addition of a convection parameterization developed by Emanuel (1991), used for most of the simulations reported here. (More specifically, we use version 1.25 of the scheme.) For comparison, we have also performed a few simulations using the scheme developed by Grell (1993), which is an upgrade of the Grell et al. (1991) scheme used in GBS, and the model's original Kuo (1974) scheme. A comparison of results using each of the schemes helps to determine the sensitivity of the behavior observed here to the convection parameterization used.

The Emanuel scheme is based on ensembles of convective updrafts and downdrafts. A key factor in the Emanuel scheme is that it requires positive buoyancy for air parcels lifted from the surface to cloud base, which is defined as the first model level above the parcels' lifting condensation level (LCL). Closely associated with this requirement is a stipulation that parcel uplift leading to convection must occur in a nonstable, or well-mixed, PBL. The PBL turbulence implied in this situation can be viewed as providing the mechanism lifting a parcel to its level of free convection. The scheme also requires the atmosphere to contain convective available potential energy (CAPE) for the initiation of convection.

When using the Grell scheme here, we have made one modification to allow the growing, small-amplitude wave to induce midlatitude convection. The Grell scheme evaluates the potential for convection in part by searching between the surface and upper troposphere for the maximum in the environment's moist static energy:

$$H = C_p T + Lq + gz, \tag{1}$$

where C_p is the heat capacity of air at constant pressure, T is temperature, L is the latent heat of vaporization, q is specific humidity, g is gravitational acceleration, and z is distance from the surface. Designating the pressure level of max(H) as $p_{\max}$, the potential for convection exists in the Grell scheme if

$$\max(\mathrm{H}) > \mathrm{H}_{\mathrm{sat}} \quad \text{for some p} \in [p_{\max} - 250 \text{ hPa}, p_{\max}], \tag{2}$$

where H_{sat} is computed using the environmental profiles in (1) but with q replaced by its saturation value. For the initial midlatitude environment, max(H) occurs in the upper troposphere and (2) is not satisfied. As the wave grows, it produces a secondary maximum near the surface, but the standard Grell scheme does not apply condition (2) to this maximum, so no midlatitude convection occurs before the wave reaches its maximum amplitude. We modified the Grell scheme to apply the test (2) using the secondary max(H) produced by the wave in the lower troposphere. With this modification, the growing wave induces midlatitude convection.

We also modified the Kuo scheme in order to allow the growing, but small amplitude, wave to provoke midlatitude convection. In this case, we reduced the critical moisture convergence the scheme requires to initiate convection to just 2% of its standard value. Also, although the Kuo scheme does not explicitly require an unstable PBL, it does check for positive parcel buoyancy at cloud base, which is again the first model layer above the LCL. Positive buoyancy at cloud base can occur more readily if the PBL is isentropic rather than dry-convectively stable so that, like the Emanuel scheme, the Kuo scheme favors a well-mixed boundary layer.

The initial states used in our experiments correspond roughly to the climatological, Southern Hemisphere winter and summer zonal average states for temperature and zonal wind. Specific humidity was modified from climatology to allow midlatitude conditional instability. Figure 2 shows distributions of zonal wind, temperature, specific humidity, and saturation equivalent potential temperature for the model's standard winter case. Compared to the winter case, the summer case (not shown) has a weaker westerly jet and near-surface meridional temperature gradient and, accordingly, weaker north–south moisture gradient. The region of potential convective instability extends farther into midlatitudes in the winter conditions state, so we give more attention here to simulations using that initial condition. The method used to ensure that our initial states are balanced is given by Branscome et al. (1989).

The waves in our experiments are initiated with a temperature perturbation superimposed on the balanced zonal mean state. The temperature perturbation has a maximum amplitude in the lowest layer and decreases

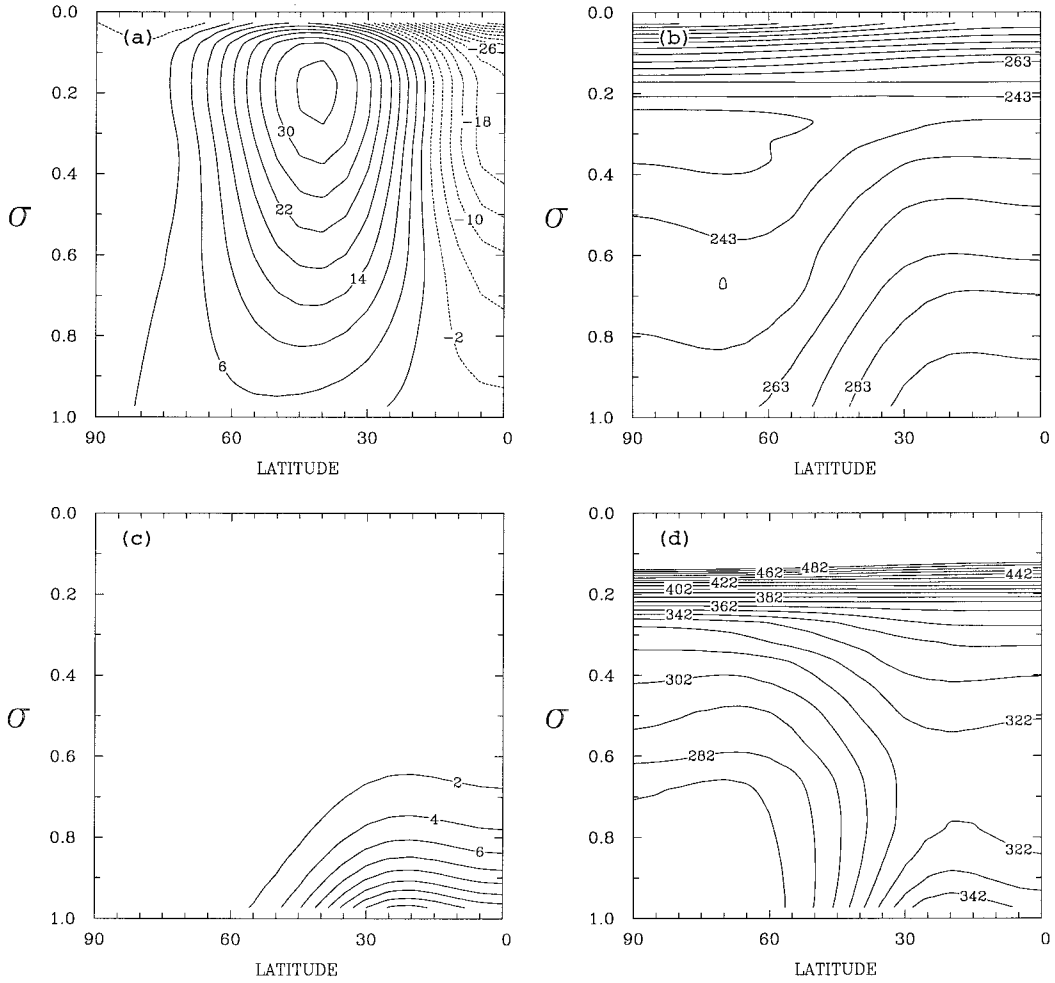

FIG. 2. Standard, winter-conditions zonal-average state for (a) zonal wind (m s^{-1}), (b) temperature (K), (c) specific humidity (g kg^{-1}), and (d) saturation equivalent potential temperature (K).

exponentially with height. The wave draws available potential energy (APE) from the zonal mean flow. In several days, a nearly exponentially growing wave emerges. Eventually nonlinear effects diminish the growth rate, and the eddy ultimately reaches a maximum amplitude (e.g., GBS). From that point, eddy kinetic energy decreases, completing the life cycle. A second life cycle may ensue. During the eddy life cycle, the energy transfer shows the usual path for baroclinically unstable waves: energy flows from zonal APE to eddy APE and then eddy kinetic energy.

We ran simulations for several different fundamental waves. Typically, zonal wavenumber 7 was the most rapidly growing and energetic, and it produced the strongest convective heating, so our discussion focuses on experiments in which zonal wavenumber 7 is perturbed. We also performed experiments in which we perturbed wavenumber 6, wavenumber 12, or wavenumber 15 in order to obtain a more complete picture of wave–convection interactions.

In the following sections, we examine the interaction of convection and eddy dynamics at different stages. The early stage is defined as the time period from the beginning to the day on which eddy kinetic energy reaches 10% of its eventual maximum. For example, the early stage of wavenumber 7 is the period from day 0 through day 7. The mature stage is defined as the rest life cycle after the early stage.

3. Temperature structure of growing waves

Analysis of the simulation output is aided by considering the vertical temperature structure of growing, baroclinically unstable waves. Figure 3 shows schematically profiles of potential temperature θ versus height in the growing wave's warm and cold sectors. The background, zonal-average potential temperature $[\theta]$ in each case is the average of the warm and cold profiles. In the lower panel, we assume that there are no fluxes of heat between the surface and the atmosphere. The magnitude of the eddy temperature field, $\theta - [\theta]$, increases toward the surface, consistent with typical linear insta-

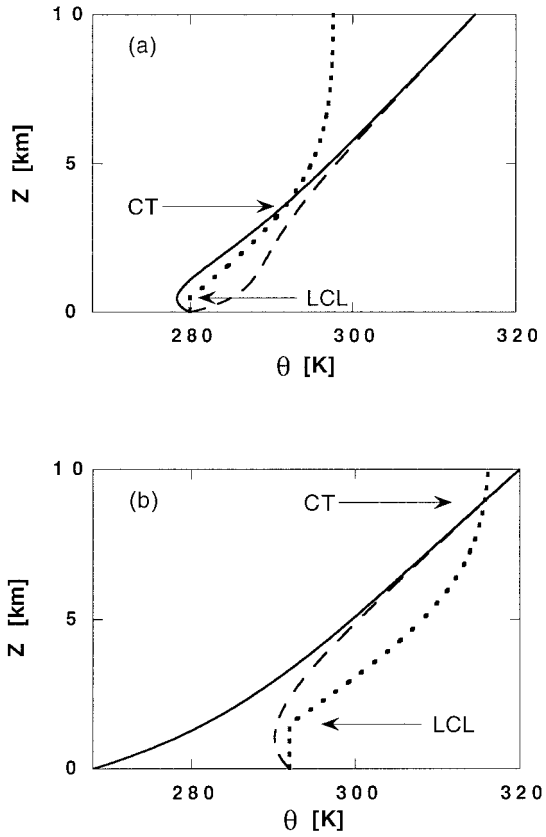

FIG. 3. Schematic diagram of potential temperature vs height in the warm (dashed line) and cold (solid line) sectors of growing waves when surface fluxes are (a) included or (b) not included in the simulation. Dotted lines are paths followed by nonentraining air parcels lifted from the surface through their lifting condensation level (LCL) and cloud top (CT).

bility computations for an external mode (e.g., Green 1960; Card and Barcilon 1982). As suggested by the figure, if the magnitude of the eddy temperature field is large enough, then an unstable boundary layer ($d\theta/dz < 0$) will develop at the surface in the warm sector. The boundary layer in the cold sector will be stable.

When surface fluxes are included, there will be an exchange of heat between the surface and the atmosphere. The surface in our simulations is the ocean, which we assume has unchanging temperature over the course of the life-cycle simulation. Surface heat fluxes tend to reduce the difference between surface and air temperatures so that the eddy temperature field is strongly damped near the surface (e.g., Branscome et al. 1989). As a consequence, an unstable boundary layer can develop in the wave's cold sector, while the warm sector remains stable (Fig. 3a). This effect of surface fluxes on the wave's near-surface temperature structure affects the distribution of convection using the Emanuel parameterization, which requires a nonstable boundary layer.

The difference in the wave's temperature structure between Figs. 3a and 3b also affects where an air parcel rising from the surface will be warmer than its surrounding environment, thus giving it positive buoyancy. Dashed lines in Fig. 3 are for a nonentraining parcel that rises from near-surface along a dry adiabat until it reaches saturation, at which point further rising occurs along a moist adiabat. When surface heat fluxes are included, nonentraining air parcels rising from the surface in either the warm or the cold sector will follow approximately the same path since near-surface air departs little from the zonal mean. Assuming that an unstable planetary boundary layer produces an isentropic environmental temperature profile near the surface, a rising parcel in Fig. 3a's cold sector will have positive buoyancy between its LCL and its cloud top (CT), defined here as the level where the nonentraining parcel becomes cooler than the environment. Positive buoyancy in this case is less likely to occur in the warm sector. In contrast, when there are no surface fluxes, only parcels rising in the warm sector are likely to attain positive buoyancy. Note also that CAPE is proportional to the vertically integrated positive buoyancy (e.g., Holton 1992). Thus, in Fig. 3, the locations where the growing wave is increasing CAPE and thus causing convective destabilization depends on whether or not surface heat fluxes are present.

4. Early stage

The results shown in Fig. 1 are from the mature phase of two life-cycle simulations. An understanding of why these differences occur can be found by examining the early stage of these and similar simulations, bearing in mind the discussion of the previous section. Using the Emanuel scheme with or without surface fluxes, the strongest convective heating in midlatitudes during the early stage occurs in the lower atmosphere (Fig. 4) and has a wavelike longitudinal structure (Figs. 5 and 6) as a consequence of the growing wave's influence on the distribution of convection.

Figure 5 shows the relationship between convective heating and features of the growing wave at the end of day 7 in the wavenumber 7 simulation with surface fluxes included. Consistent with the discussion in section 3, the moist convection occurs in the cold sector of the wave, where in the presence of surface heat flux, the boundary layer has become dry convectively unstable. Figure 6 shows the same relationships for a simulation identical to that producing Fig. 5, but with no surface fluxes included. Again consistent with section 3, the moist convection in this simulation occurs in the warm sector, which now has the unstable boundary layer. It also occurs primarily in the region of positive low-level vertical motion, consistent with the assumption coupling convection to low-level upward motion that was used in the previously cited analytical studies. Note that, while some of the analytical studies included surface momentum flux (friction), none included surface

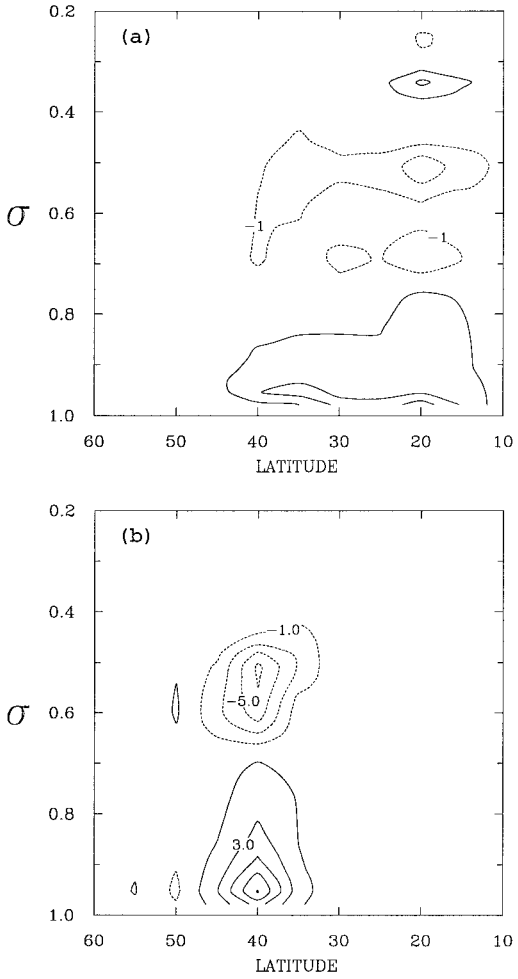

FIG. 4. Latitude–height cross section of convective heating produced by the Emanuel scheme during the last hour of day 7 for two wavenumber 7 runs that (a) include or (b) do not include surface fluxes. Units are (a) 10^{-1} K day^{-1} and (b) 10^{-2} K day^{-1}. Contour interval in each panel is 2 units, with solid contours denoting positive values.

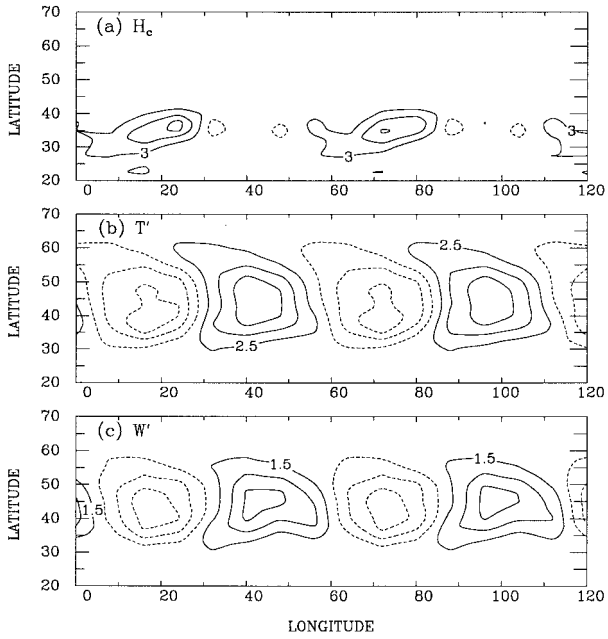

FIG. 5. Latitude–longitude contours of (a) convective heating (10^{-1} K day^{-1}), (b) eddy temperature (10^{-1} K), and (c) eddy vertical velocity (10^{-4} m s^{-1}) for 960 hPa at the end of day 7, from a wavenumber 7 run including Emanuel convection and surface fluxes. Contour intervals are (a) 0.6 K day^{-1}, (b) 0.5 K, and (c) 3×10^{-4} m s^{-1}, with dashed contours denoting negative values.

sensible heat flux, which produces the differences in temperature structure between Figs. 3a and 3b.

The Emanuel scheme requires that there be CAPE present for convection to initiate. In a model with discrete vertical layers, the Emanuel scheme's CAPE for a parcel rising from cloud-base layer (NCB) to the cloud-top layer (NCT) is

$$\text{CAPE} = \sum_{n=\text{NCB}}^{\text{NCT}} R_d(T_{vp}^n - T_v^n)\Delta_n \ln p, \qquad (3)$$

where R_d is the gas constant for dry air, T_{vp}^n is the cloud virtual temperature for an air parcel lifted from the lowest model layer to layer n, T_v^n is the environment's virtual temperature in layer n, and $\Delta_n \ln p$ is the change in log(pressure) across layer n. The CAPE thus depends on the difference between the environmental virtual temperature profile and the cloud virtual temperature

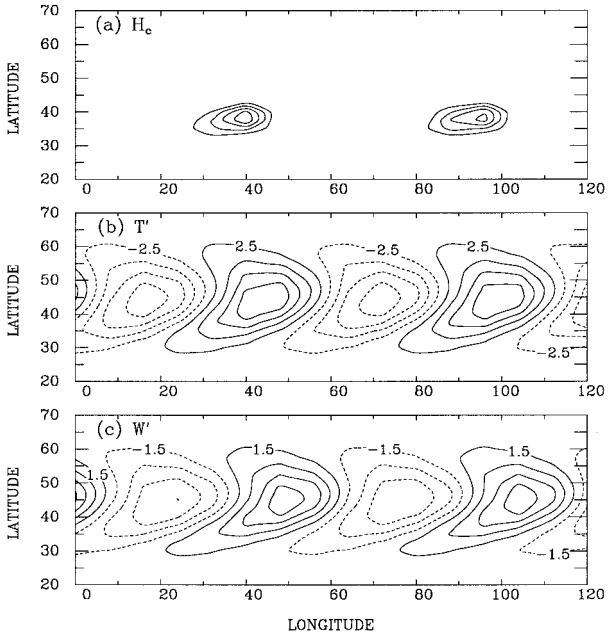

FIG. 6. As in Fig. 5 but with no surface fluxes included. Contour intervals are (a) 0.1 K day^{-1}, (b) 0.5 K, and (c) 3×10^{-4} m s^{-1}, with dashed contours denoting negative values.

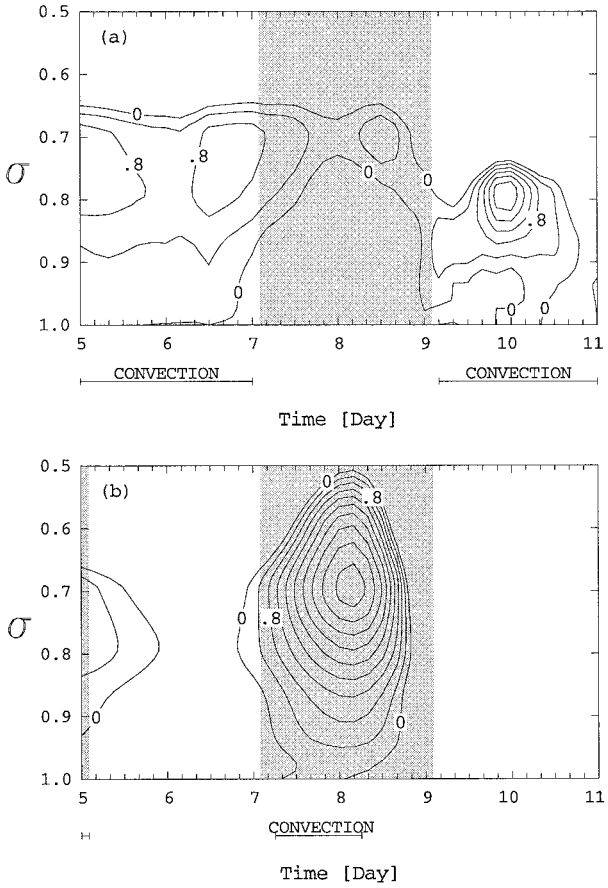

FIG. 7. Time–height contours of positive ($T_{vp} - T_v$) (K) for a point at 42° latitude in wavenumber 7 runs that (a) include and (b) do not include surface fluxes. The contour interval is 0.4 K. Horizontal I-bars mark when convection is occurring at this point. Shading marks when the point is in the wave's warm sector.

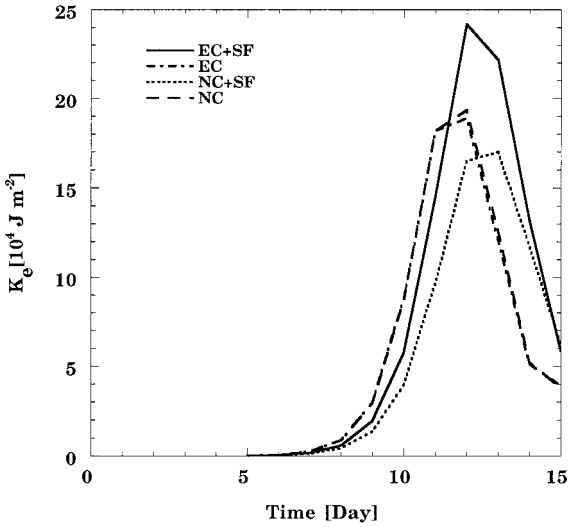

FIG. 8. Plot of K_e vs time for runs that include Emanuel convection and surface fluxes (EC + SF), Emanuel convection and no surface fluxes (EC), surface fluxes and no convection (NC + SF), and no convection or surface fluxes (NC).

profile. Figure 7 shows time–height contour plots of positive values of $T^n_{vp} - T^n_v$ for one point at latitude 42° in two wavenumber 7 runs, one with and one without surface fluxes. Consistent with the discussion in section 3, the location of CAPE development is strongly dependent on whether or not surface fluxes are included in the simulation, with the production of CAPE favored in the cold sector when surface fluxes are present. Also consistent with Fig. 3a, when surface fluxes are present, the warm sector's layer of positive $T^n_{vp} - T^n_v$ occurs well above the surface. Finally, the figure shows that the cloud-top level tends to be higher when no surface fluxes are present, a feature that one might also infer from Fig. 3. We shall see when examining the mature stage of wave development that this difference in cloud-top height is important for how the Emanuel scheme's convection enhances wave growth when surface fluxes are present.

For simulations using either the modified Grell or modified Kuo schemes, the location of convection is also governed by whether or not the simulation includes surface fluxes. As with the Emanuel scheme, when no surface fluxes are present, midlatitude convection using either scheme occurs in the warm sector, whereas when surface fluxes are included convection occurs in the cold sector. For the Grell scheme, the critical factor is the shift of atmospheric destabilization by nonconvective processes from the warm sector to the cold sector. The measure of destabilization in the Grell scheme is based on the time change of $\max(H) - H_{\text{sat}}$ and so is not precisely the same as destabilization determined from the time change of $T^n_{vp} - T^n_v$. However, the two differences are similar enough that Fig. 7 gives an approximate indication of where the Grell scheme would find atmospheric destabilization, which would tend to occur where $T^n_{vp} - T^n_v$ is increasing with time. (The reader is reminded that Fig. 7 includes the effects of convective heating on the temperature profile and so includes convective stabilization as well as nonconvective destabilization.) The shift in the location of destabilization is also important for the Kuo scheme, as is the shift of the unstable boundary layer from the warm to cold sector when surface fluxes are added. Finally, for all three schemes, convection is shallower when surface fluxes are included.

5. Mature stage

a. Enhanced wave growth

During the mature stage, the wave attains its maximum amplitude before decaying. Figure 8 shows the evolution of eddy kinetic energy K_e for the two wavenumber 7 simulations using the Emanuel scheme with and without surface fluxes. Also shown in Fig. 8 is the evolution of K_e for two additional runs with and without surface fluxes that used no convection scheme. For the

latter two simulations, adding surface fluxes reduces the maximum K_e attained by the wave, which might be expected since surface momentum and sensible heat fluxes suppress the wave's amplitude near the surface (e.g., Branscome et al. 1989). However, for the two runs with convection included, adding surface fluxes increases the maximum K_e by 28%, so convection is somehow enhancing wave growth.

One possibility is that convective heating supplies energy directly to the wave. However, for the two simulations without surface fluxes, maximum K_e hardly depends on whether or not convection is included. In the runs that include convection, the generation of available potential energy by convection, whether in the warm or the cold sector, has an absolute value less than 0.03 W m^{-2} when averaged over days 8–14, whereas the conversion of zonal to eddy available potential energy averages more than 0.9 W m^{-2} during the same period. Thus, the direct effect of convective heating on wave development is negligible.

Figure 4 shows midtroposphere cooling by convection, which is occurring in the cold sector. This cooling is caused by downdrafts in the Emanuel scheme and partially balances the midtropospheric heating caused by the eddy vertical heat flux. In the warm sector of the wave, heating by large-scale condensation promotes wave growth by catalyzing stronger upward motion and thus a stronger conversion of APE (GBS). Conceivably, the convective cooling in the cold sector could accomplish similar results. We performed additional computations in which this cooling was not applied to the resolved temperature field. The absence of the cooling had a negligible effect on the wave's development.

Figure 4 shows that the lower tropospheric heating occurs primarily within and just above the model's planetary boundary layer. This location suggests that the cold-sector convection could modify the PBL in a way that enhances wave growth, for example, by reducing temperature-wave damping by surface heat fluxes. We examine this possibility by reconsidering the early stage, when the eddy fields have relatively small magnitude, so that we can assume approximately linear dynamics. Then, the eddy potential temperature field θ' is the sum of two fields:

$$\theta' = \theta'_w + \theta'_c, \tag{4}$$

where θ'_w is the eddy potential temperature due to the growing baroclinic wave and θ'_c is the eddy potential temperature due to accumulated convective heating. We assume that the effect of moisture condensation is to modify the dry instability during the early stage, but not produce a dramatically different behavior (e.g., GBS), so that θ'_c represents a small addition to θ'_w and the wave speeds during the early stage are not substantially changed by the condensation. The eddy potential temperature tendency during the early stage is then, in Cartesian geometry,

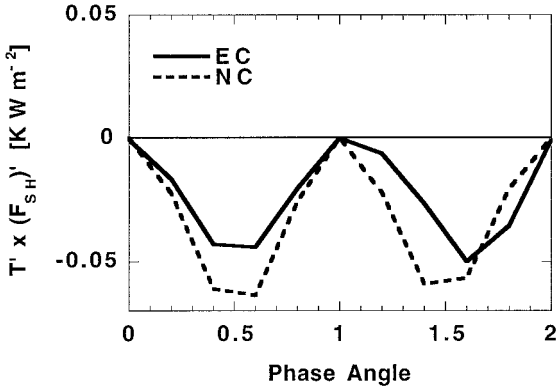

FIG. 9. The product $(F_{sh})'T'$ in the model's lowest layer as a function of wave phase angle. Results are at 42° latitude on day 5 for wavenumber 7 runs with surface fluxes that include Emanuel convection (EC) or have no convection (NC). The phase angle is in units of π, and the warm sector occurs for phase angle $\in$ [0, 1].

$$\frac{\partial \theta'}{\partial t} = \left\{ -[u]\frac{\partial \theta'_w}{\partial x} - v'_w\frac{\partial [\theta]}{\partial y} - w'_w\frac{\partial [\theta]}{\partial z} \right\} - [u]\frac{\partial \theta'_c}{\partial x} + \frac{[\theta]}{[T]}\dot{H}'_c, \tag{5}$$

where the brackets refer to the zonal-average field, the subscript w refers to baroclinic wave variables, and H'_c is the eddy part of the convective heating. Other new symbols in (5) have their standard meteorological definitions. The term in braces in (5) represents the evolution of the temperature field due to the growing wave. In addition to temperature-wave growth, it also produces a propagation of the θ' wave downstream (toward the east) with a phase speed of roughly 10 m s^{-1} in midlatitudes.

The convective terms distort the temperature wave, with the advection of θ'_c in particular inducing a phase lag that varies with height within the PBL. The distortion is sufficient to further stabilize the PBL over part of the already stable warm sector, where PBL structure is not governed by dry convection. As a consequence, damping of the temperature wave by surface sensible heat flux F_{sh} is reduced. The damping affects wave energetics through the generation of eddy available potential energy, for which F_{sh} alone gives a contribution,

$$G_e \propto (F_{sh})'T'_s, \tag{6}$$

where T'_s is the eddy temperature field in the model's lowest layer. The magnitude of this product is substantially reduced in the wave's warm sector when Emanuel convection is included (Fig. 9). Integrated across the wave, the sink of eddy available potential energy is 20%–30% smaller as the wave grows. The quantitative response of G_e to the convective heating and surface flux is likely sensitive to details of the PBL parameterization used here, so further examination of this issue is beyond the scope of this study. This process, however,

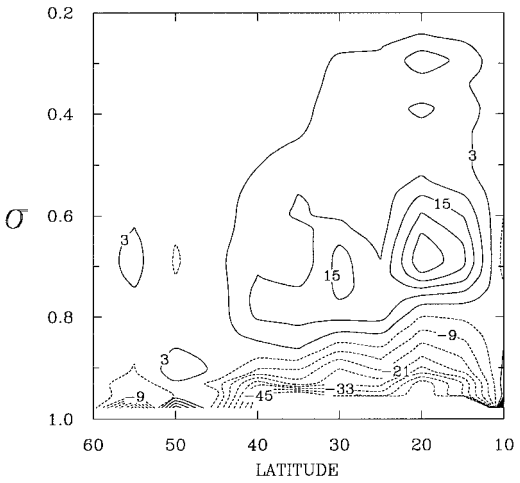

FIG. 10. Latitude–height cross section of moistening rate by Emanuel convection during the last hour of day 7 for the wavenumber 7 run that includes surface fluxes. Contour interval is $6 \cdot 10^{-2}$ g kg^{-1} day^{-1}, with dashed contours denoting negative values. (Contours less than -45×10^{-2} g kg^{-1} day^{-1} are not drawn.)

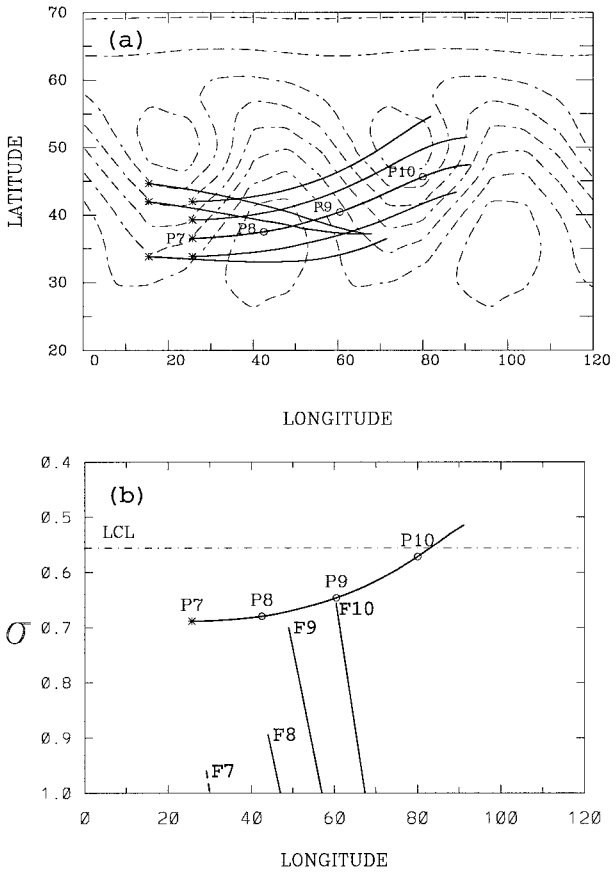

FIG. 11. Paths of particles released where the largest convective moistening was occurring at the end of day 7 in the run using Emanuel convection and surface fluxes: (a) latitude–longitude paths for all particles, and (b) latitude–height path for one of the particles. The particle location at the end of days 7–10 is marked P7, . . . , P10 for the path appearing in both panels. Panel (a) also shows contours of surface pressure (dash–dot lines) at the end of day 10 (cf. Fig. 1a for contour values). Panel (b) also shows the lifting condensation level (LCL; dash–dot line) for air parcels at the path's origin and vertical lines marking the location and vertical extent of the cold front at the particle's latitude on days 8, 9, and 10, denoted by F8, F9, F10, and the boundary between the warm and cold sectors on day 7 (dashed line F7).

only removes a sink of wave energy due to surface heat flux, and by itself it could at best increase the maximum K_e from 1.7×10^5 J m^{-2} (the no convection case with surface fluxes) to 1.9×10^5 J m^{-2} (the no convection case without this or other surface sinks). An additional source of energy is needed.

A source of additional energy can result from surface evaporation, if the water vapor given to the atmosphere condenses appropriately. All three convective schemes condense some of this water into surface precipitation, even when the convection is relatively shallow, but we have seen that such direct condensational heating by the Emanuel scheme is of negligible importance to wave energetics. However, the Emanuel scheme also transports water vertically from the boundary layer into the lower troposphere (Fig. 10). The moistening shown in Fig. 10 occurs in the cold sector. If this added water condensed there, it would produce a loss rather than gain of eddy APE.

To determine if and where the water added to the cold sector does condense, we have performed tracer computations using the resolved, three-dimensional wind fields of the simulation. The tracers track the paths of particles released at extratropical grid points experiencing convection at the end of days 5, 6, . . . , 10 in the run using Emanuel convection and surface fluxes. For each grid point so chosen, the particle was released at the level with the largest convective moistening rate. We computed particle paths following the method of Kida (1983), except that we used the model-computed winds from every time step (15 min) of the simulation.

Figure 11a shows the latitude–longitude paths for particles released at the end of day 7. Recall that Fig. 5 shows horizontal distributions of convective heating and eddy temperature on day 7, thus indicating the atmospheric state at release time. Note, however, that Fig. 5 shows fields at 960 hPa, whereas maximum convective moistening, and thus particle release, occurs near 700 hPa. Figure 11a also shows contours of surface pressure at the end of day 10 to indicate the synoptic state near the ending time of the trajectories. (Fig. 1a gives further detail of the synoptic state at this time.) Figure 11b shows the height–longitude path for a particle originating at a point with one of the largest convective moistening rates. The vertical axis is the model's sigma coordinate. The vertical motion of this particle is representative of its neighbors in Fig. 11a that also follow a northeastward path. Figure 11b also shows the LCL for air at the particle's origin, as well as the location of the cold front in the lower atmosphere at the particle's latitude for the times marked. We have defined the cold

TABLE 1. Atmospheric properties at the end of days 7–10 along the trajectory appearing in both Figs. 11a and 11b. Properties shown are potential temperature (θ), equivalent potential temperature (θ_e), temperature (T), relative humidity (RH), and lifting condensation level (LCL).

Day	θ (K)	θ_e (K)	T (K)	RH (%)	LCL (hPa)
7	296.7	307.1	267.7	34	584
8	296.7	306.5	266.6	37	583
9	297.0	304.7	262.7	47	574
10	297.7	302.1	253.9	75	547

front here as the boundary between positive and negative eddy temperature at levels where the temperature contrast between the centers of the warm and cold sectors exceeds 5°C. This boundary is the location of strongest temperature gradient. By this definition, temperature contrasts on day 7 are not strong enough to produce a front, but we have drawn on the figure the boundary dividing warm and cold sectors in the lower atmosphere. The fronts weaken and eventually disappear with height because the amplitude of the eddy temperature field decreases with height [cf. Fig. 7 of Branscome et al. (1989)].

The horizontal trajectories in Fig. 11a are qualitatively similar to those computed by others for particles released in the lower troposphere upstream from an extratropical cyclone (cf. Kuo et al. 1985; Merrill et al. 1986; Reed et al. 1992). We assume that these trajectories correspond to the paths that water vapor follows from the same starting points. To verify this, we have diagnosed potential and equivalent potential temperatures along the trajectories. Table 1 shows these quantities for the trajectory appearing in both Figs. 11a and 11b. The potential and the equivalent potential temperatures are fairly constant (cf. Reed et al. 1992) and exhibit changes much smaller than the spatial variation of these fields across the midlatitudes. The results in Table 1 are representative for all the trajectories shown, so we conclude that they do represent paths followed by water vapor from the point where convection injects it into the lower troposphere to where it condenses.

Table 1 and Fig. 11b also show that air moving along this trajectory rises, cools, and approaches saturation as it progresses; its water vapor starts condensing during day 11. In addition, its path takes it from the cold sector, over the front, and into the warm sector (Fig. 11b). The overall behavior is representative of moist air parcels following the trajectories parallel to this one in Fig. 11a. Similar trajectories appear in some observational studies of extratropical storms (e.g., Browning and Harrold 1969; Browning et al. 1973; Harrold 1973). Model parcels following trajectories like that in Fig. 11b experience condensation in the warm sector by large-scale uplift. Parcels following paths originating in layers convectively moistened at the end of days 6 and 8 may also reach their LCL and tend to do so between days 10 and 12, whereas air parcels following paths starting at the end of days 5, 9, and 10 do not reach their LCL while the wave is still growing. Water vapor pumped by the Emanuel scheme into the cold sector's lower troposphere during days 7 through 8 thus condenses later in the warm sector during the period when the wave is growing toward the largest K_e of the cases depicted in Fig. 8. The additional heating increases the generation of available potential energy by large-scale condensation.

The net change in generation, however, is an order of magnitude smaller than changes experienced by the conversion terms in the wave's energy cycle when Emanuel convection is added. A more important effect of the added moisture thus appears to be its impact on the conversion of eddy available to eddy kinetic energy. The added moisture enters the warm sector in a layer roughly coincident with the levels of strongest eddy vertical motion (approximately 500–700 hPa, not shown). The importance of the additional moisture at these levels can be seen by considering the conversion of eddy available (A_e) to eddy kinetic energy:

$$C\{A_e, K_e\} = -\int \frac{R_d}{p}[\omega' T']\, dm, \qquad (7)$$

where $[\omega' \mathrm{T}']$ is the zonal-average eddy vertical heat flux, dm is the differential mass element for the atmosphere, and the integration occurs over the entire model atmosphere. In GBS, it was shown that the condensational heating caused by large-scale uplift catalyzes a stronger $C\{A_e, K_e\}$ by enhancing the buoyancy of the air and, hence, the vertical eddy heat flux $[\omega' \mathrm{T}']$ appearing in (7). As a consequence, the additional moisture provided by shallow convection amplifies the tendency found in GBS for large-scale supersaturation to catalyze a more energetic life cycle and yield a larger maximum in eddy kinetic energy. The conversion $C\{A_e, K_e\}$ is 30% larger in the run with convection and surface fluxes than in the run with surface fluxes only.

The ability of the Emanuel scheme's convection to amplify the wave's energy cycle rests on the fact that the convection is relatively shallow in simulations with surface fluxes included. The warm-sector convection that occurs when surface fluxes are absent also moistens part of the atmosphere, but as the wave matures, the moistening in the region 30°–60°, where the vertical eddy heat flux in (7) is strongest, is two orders of magnitude smaller than the moistening in Fig. 10, so the warm-sector convective moistening has little influence on $C\{A_e, K_e\}$. The occurrence of surface evaporation directly below the convection is also important. In a wavenumber 7 run that excluded surface evaporation while retaining convection, surface drag, and surface sensible heat flux, the large-scale supersaturation was reduced and $C\{A_e, K_e\}$ was 32% smaller than in the simulation that included surface evaporation.

The modified Grell and Kuo schemes also give relatively shallow convection in the cold sector when sur-

TABLE 2. Moistening rate by convection averaged over the region 30°–60° lat and 800–500 hPa for runs including surface fluxes and using different convection schemes. Rates shown are averages over the last hour of the day indicated.

Convection scheme	Moistening rate (10^{-2} g kg^{-1}/day)		
	Day 6	Day 7	Day 8
Emanuel	2.3	2.5	1.2
Grell	0.0	0.1	0.0
Kuo	1.4	−1.0	−1.0

face fluxes are included, but neither scheme prompts the increase in K_e observed when using the Emanuel scheme. The critical difference appears to be the degree of lower-troposphere moistening each scheme produces. Table 2 shows the moistening rate by convection for the layer 800–500 hPa in midlatitudes from runs using each scheme. The moistening rate is given for days 6–8, when the Emanuel scheme moistens the lower troposphere with water vapor that later condenses in the warm sector. The reasons for the differences in moistening rate by each convective scheme lie within the details of each convective parameterization and are beyond the scope of this study. However, Table 2 and the trajectory discussion above indicate that the key difference between schemes in their ability to enhance eddy kinetic energy is their amount of tropospheric moistening in the cold sector above the PBL.

b. Convection lagging wave development

Net convective heating averaged over latitudes 20°–70° typically reaches its maximum in the mature stage one or two days after the eddy kinetic energy has passed its maximum. This behavior was also noted in GBS. To understand this lag, we analyze how the potential for instability in the atmosphere evolves over the life cycle, focusing on the Emanuel scheme's convection. To diagnose the potential for convective instability, we have calculated the saturation equivalent potential temperature θ_e, computed as

$$\theta_e = \theta \exp\left\{\frac{Lq_s}{c_p T}\right\}, \tag{8}$$

where L is the latent heat of vaporization, q_s is the saturation specific humidity, and c_p is the heat capacity of air at constant pressure. An atmospheric column is potentially unstable to convection when θ_e decreases with height somewhere in a statically stable atmospheric column (Emanuel 1994). This behavior is most likely to occur in the lower atmosphere where the decrease with height of relatively warm temperatures allows q_s to decrease rapidly enough to override the general increase of θ with height.

We diagnose potential convective instability here by the difference

$$\Delta\theta_e = [\theta_e](850 \text{ hPa}) - [\theta_e](1000 \text{ hPa}). \tag{9}$$

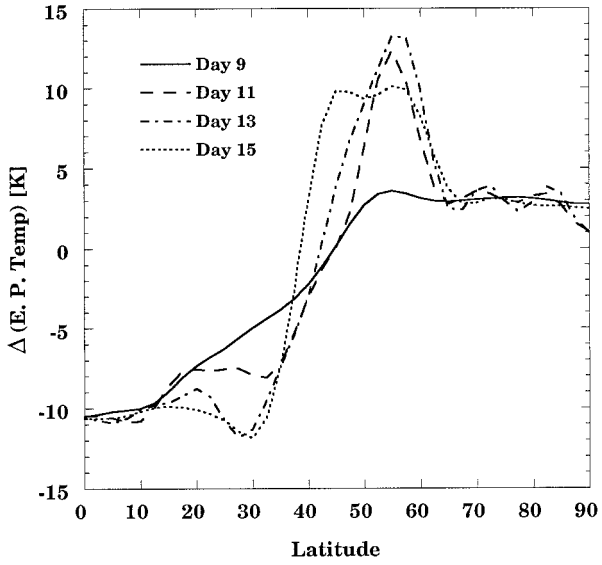

FIG. 12. Plot of $\Delta\theta_e$ vs latitude for selected times in the wavenumber 7 run using Emanuel convection.

Figure 12 shows $\Delta\theta_e$ as a function of latitude for selected times during the wavenumber 7 run using the Emanuel scheme. During the mature stage, static stability in midlatitudes increases, a behavior occurring as part of the baroclinic adjustment process (Stone 1978; Gutowski et al. 1989). Midlatitude convection is thus suppressed simply because the overall stability of the atmosphere increases at these latitudes. More important, however, is the decrease in convective stability induced by the wave dynamics in the neighborhood of 30° latitude, especially between days 11 and 13. Despite the strong destabilization being produced by the eddy dynamics, the convective maximum does not occur during this period but later, as the eddy dynamics weaken.

Convection requires sufficient moisture to occur in addition to potential instability. We can investigate moisture change during the life cycle through the distribution of vertically integrated specific humidity. Figure 13 gives the change in atmospheric humidity from day 0 to selected days in the wavenumber 7 simulation. The eddy moisture flux (e.g., Fig. 12 of GBS) draws moisture from the subtropics and transports it poleward as the wave grows. As a result, atmospheric moisture increases in the region 40°–60° but decreases between roughly 30°–40° as the wave grows. Latitudinal moisture transport to support subtropical convection is thus lacking as the wave grows to maximum amplitude. Moisture is deposited where the atmosphere is stabilized in midlatitudes and is depleted or increases very little where destabilization occurs. Lowered moisture in the subtropics produces a higher LCL, making convection less likely (cf. Fig. 3). Thus, the net effect of the wave dynamics in both the subtropics and midlatitudes during the period of wave growth is a suppression of convection relative to its strength as the wave weakens.

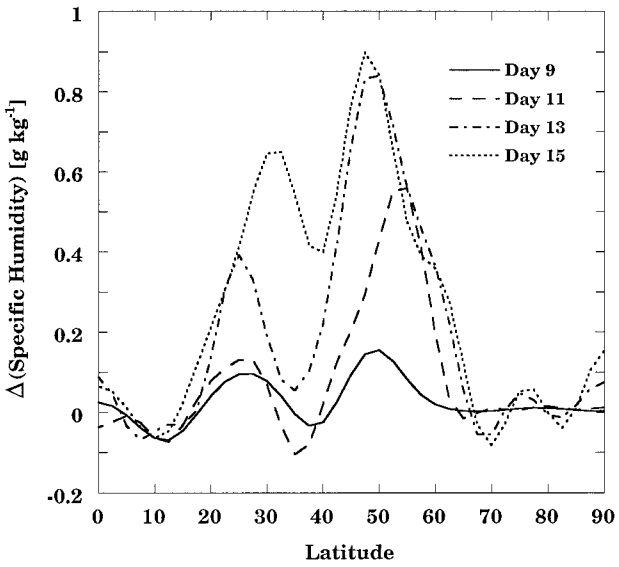

FIG. 13. As in Fig. 12 but for the change from the initial state in zonal and vertical average specific humidity.

Surface evaporation in the subtropics can counteract the depletion by eddy dynamics, but up through day 11 it is insufficient to prevent a reduction in atmospheric humidity near 30°. As the wave decays, however, its horizontal moisture flux decreases rapidly and surface evaporation near 30° not only restores lost humidity but also helps increase it well beyond its initial amount. The increased humidity lowers the lifting condensation level and allows convection to reach its largest total magnitude while the wave decays.

6. Summary and discussion

We have examined the role of convection in the dynamics of the eddy life cycle through numerical experiments using an ocean-covered lower boundary with zonally symmetric temperature distribution. The initial and boundary conditions are based on Southern Hemisphere climatology, except that initial specific humidity was modified from climatology to allow midlatitude conditional instability. As in GBS, we focus on transient eddy processes contributing to global-scale circulation and climate. The behavior of life cycles for wavenumber 7 has been emphasized in our work because it is the most unstable wave and it attains the largest amplitude, thus producing the strongest eddy fluxes of heat, moisture, and momentum in the extratropical atmosphere. Other wave scales may contribute to transient eddy transports and modification of the zonal mean state, so we also performed experiments using wavenumber 6, 12, or 15 as the fundamental wave in order to cover a range of wavenumbers. Our results obtained here apply qualitatively to both winter and summer simulations and to all wavenumbers studied except that the amplification of K_e that occurs when using the Emanuel scheme is much stronger for wavenumber 7 than for other wavenumbers.

The growth of the unstable wave prompts the appearance of midlatitude convection. However, there are substantial differences in the character of convection between simulations with and without surface fluxes included. These differences are tied to how the wave's near-surface temperatures evolve under the influence of the growing wave and, when included, surface sensible heat flux, with the location of moist-convective destabilization being strongly dependent on the influence of both processes, as outlined schematically in Fig. 3. As a consequence, for all three convective schemes used here (Emanuel, modified Grell, modified Kuo), convection is favored in the warm sector when there are no surface fluxes included in the simulation and in the cold sector when there are. Each scheme's convection is also shallower (though still precipitating) when it occurs in the cold sector rather than the warm sector, with convective heating and moistening confined to the lower troposphere.

The shallowness of the cold-sector convection, however, is important for enhanced wave growth induced by the Emanuel scheme when surface fluxes are present. The relatively shallow convection plays a central role in a water cycle wherein 1) evaporation gives moisture to the cold sector's boundary layer, 2) convection pumps some of the moisture into the lower troposphere above the boundary layer, 3) the large-scale circulation transports the moisture eastward and upward into the wave's warm sector, and 4) stable condensation precipitates the moisture out of the atmosphere. The added moisture enhances a process described in GBS wherein heating by supersaturation in the lower to middle troposphere catalyzes a more energetic life cycle by inducing greater conversion of available potential energy to kinetic energy. The enhancement observed here is parameterization dependent, and the key factor appears to be how much lower tropospheric moistening each scheme produces. The modified Grell and Kuo schemes give much less lower-tropospheric moistening, so they do not promote greater wave growth like the Emanuel scheme does. These simulations are of course for an idealized environment, as indicated by the 2-day episodes of continuous convection experienced by the midlatitude point in Fig. 7. We are examining more complex environments using a variety of convection schemes to discern whether or not this water cycle does indeed contribute to the development of observed, marine storms.

These simulations have also been performed at relatively low resolution, especially in the zonal direction. However, as noted, the behavior of particle paths traced here appears to be realistic in comparison with observations. Additional paths (not shown) that originate lower in the cold sector's troposphere also show realistic behavior, moving southeastward and toward the surface and then veering to the southwest near the surface cold front. For the spectral truncation used, the model may

not resolve well the vertical extent of the cold front (Fig. 11b), so the model's flow may allow more air to reach the warm sector than is typical. In addition, the model's truncated spectral representation potentially could smear fields such as convective moistening, producing an effective moisture transport across the cold front that has no physical basis. However, an examination of transformed convective moistening (not shown) shows that any such nonphysical transport across the front is very small.

The location of convection in our computations is consistent with the assumed location in the analytic studies listed in the introduction. In those studies, convection is assumed to occur where the vertical velocity in the lower atmosphere is upward. This behavior also occurs for each of the convection schemes used here when there are no surface fluxes included in the simulation (Fig. 6). The common factor among all the analytic and numerical computations is that none include surface sensible heat flux. When surface fluxes are included, their influence on convective destabilization leads to convection occurring where the wave's vertical velocity in the lower atmosphere is downward (Fig. 5). Thus, surface–atmosphere coupling by sensible heat flux may be more important for inducing convection than the wave's large-scale vertical motion field when there is a strong heat flux coupling between the surface and the atmosphere. This suggests an alternative linear instability analysis in which large-scale destabilization for convection is tied to the coupled influence of the wave and surface fluxes on near-surface temperature. We are currently exploring this approach for linking convection to baroclinic wave instability.

Acknowledgments. We thank the Air Force Phillips Laboratory and Atmospheric and Environmental Research, Inc., for providing us with the PL/GD-AER global spectral model with PBL updates that was used for these computations. We also thank K. Emanuel for making available his convection code and L. Branscome, D. Stewart, T.-C. Chen, J. Stanford, C. Snyder, and anonymous reviewers for helpful comments in the course of completing this work. This research was supported by NSF Grants ATM-913522 and ATM-9616811 to Iowa State University and by an Iowa State Office of the Provost Global-Change Assistantship.

REFERENCES

Balasubramanian, G., and M. K. Yau, 1994: Baroclinic instability in a two-layer model with parameterized slantwise convection. *J. Atmos. Sci.,* **51,** 971–990.

Bannon, P. R., 1986: Linear development of quasi-geostrophic baroclinic disturbances with condensational heating. *J. Atmos. Sci.,* **43,** 2261–2274.

Branscome, L. E., W. J. Gutowski, and D. A. Stewart, 1989: Effect of surface fluxes on the nonlinear development of baroclinic waves. *J. Atmos. Sci.,* **46,** 460–475.

Browning, K. A., and T. W. Harrold, 1969: Air motion and precipitation growth in a wave depression. *Quart. J. Roy. Meteor. Soc.,* **95,** 288–309.

——, M. E. Hardman, T. W. Harrold, and C. W. Pardoe, 1973: The structure of rainbands within a mid-latitude depression. *Quart. J. Roy. Meteor. Soc.,* **99,** 215–231.

Card, P. A., and A. Barcilon, 1982: The Charney stability problem with a lower Ekman layer. *J. Atmos. Sci.,* **39,** 2128–2137.

Chang, S. W., T. R. Holt, and K. D. Sashegyi, 1996: A numerical study of the ERICA IOP4 marine cyclone. *Mon. Wea. Rev.,* **124,** 27–46.

Charney, J. G., and A. Eliassen, 1964: On the growth of the hurricane depression. *J. Atmos. Sci.,* **21,** 68–75.

Emanuel, K. A., 1991: A scheme for representing cumulus convection in large-scale models. *J. Atmos. Sci.,* **48,** 2313–2335.

——, 1994: *Atmospheric Convection.* Oxford University Press, 580 pp.

——, M. Fantini, and A. J. Thorpe, 1987: Baroclinic instability in an environment of small stability to slantwise moist convection. Part I: Two-dimensional models. *J. Atmos. Sci.,* **44,** 1559–1573.

Fantini, M., 1990: Nongeostrophic corrections to the eigensolutions of a moist baroclinic instability problem. *J. Atmos. Sci.,* **47,** 1277–1287.

Green, J. S. A., 1960: A problem in baroclinic instability. *Quart. J. Roy. Meteor. Soc.,* **86,** 237–251.

Grell, G. A., 1993: Prognostic evaluation of assumptions used by cumulus parameterizations. *Mon. Wea. Rev.,* **121,** 764–787.

——, Y.-H. Kuo, and R. J. Pasch, 1991: Semiprognostic tests of cumulus parameterization schemes in the middle latitudes. *Mon. Wea. Rev.,* **119,** 5–31.

Gutowski, W. J., L. E. Branscome, and D. A. Stewart, 1989: Mean flow adjustment during life cycles of baroclinic waves. *J. Atmos. Sci.,* **46,** 1724–1737.

——, ——, and ——, 1992: Life cycles of moist baroclinic eddies. *J. Atmos. Sci.,* **49,** 306–319.

Gyakum, J. R., 1983a: On the evolution of the *QE II* storm. I: Synoptic aspects. *Mon. Wea. Rev.,* **111,** 1137–1155.

——, 1983b: On the evolution of the *QE II* storm. II: Dynamic and thermodynamic structure. *Mon. Wea. Rev.,* **111,** 1156–1173.

Harrold, T. W., 1973: Mechanisms influencing the distribution of precipitation within baroclinic disturbances. *Quart. J. Roy. Meteor. Soc.,* **99,** 232–251.

Holton, J. R., 1992: *An Introduction to Dynamic Meteorology.* Academic Press, 511 pp.

Jiang, W., 1994: The role of convection in eddy life cycles. M.S. thesis, Dept. of Geological and Atmospheric Sciences, Iowa State University, 86 pp. [Available from UMI, P.O. Box 1346, Ann Arbor, MI 48106-1346; available online from http://www.umi.com.]

Kida, H., 1983: General circulation of air parcels and transport characteristics derived from a hemispheric GCM. Part 1. A determination of advective mass flow in the lower stratosphere. *J. Meteor. Soc. Japan,* **61,** 171–187.

Kuo, H. L., 1974: Further studies of the parameterization of the influence of cumulus convection on large-scale flow. *J. Atmos. Sci.,* **31,** 1232–1240.

Kuo, Y.-H., and S. Low-Nam, 1990: Prediction of nine explosive cyclones over the western Atlantic Ocean with a regional model. *Mon. Wea. Rev.,* **118,** 3–25.

——, M. Skumanich, P. L. Haagenson, and J. Chang, 1985: The accuracy of trajectory models as revealed by observing system simulation experiments. *Mon. Wea. Rev.,* **113,** 1852–1867.

——, M. A. Shapiro, and E. G. Donall, 1991: The interaction between baroclinic and diabatic processes in a numerical simulations of a rapidly intensifying extratropical marine cyclone. *Mon. Wea. Rev.,* **119,** 368–384.

Mak, M., 1982: On moist quasi-geostrophic baroclinic instability. *J. Atmos. Sci.,* **39,** 2028–2037.

——, 1983: On moist quasi-geostrophic baroclinic instability in a general model. *Sci. Sin.,* **B26,** 850–864.

——, 1994: Cyclogenesis in a conditionally unstable moist baroclinic atmosphere. *Tellus,* **46A,** 14–33.

Merrill, J. T., R. Bleck, and D. Boudra, 1986: Techniques of Lagrangian trajectory analysis in isentropic coordinates. *Mon. Wea. Rev.,* **114,** 571–581.

Moorthi, S., and A. Arakawa, 1985: Baroclinic instability with cumulus heating. *J. Atmos. Sci.,* **42,** 2007–2031.

Ooyama, K., 1964: A dynamical model for the study of tropical cyclone development. *Geofis. Int.,* **4,** 187–198.

Reed, R. J., M. T. Stoelinga, and Y.-H. Kuo, 1992: A model-aided study of the origin and evolution of the anomalously high potential vorticity in the inner region of a rapidly deepening marine cyclone. *Mon. Wea. Rev.,* **120,** 893–913.

Smith, P. J., P. M. Dare, and S. Lin, 1984: The impact of latent heat release on synoptic-scale vertical motions and the development of an extratropical cyclone system. *Mon. Wea. Rev.,* **112,** 2421–2430.

Stone, P. H., 1978: Baroclinic adjustment. *J. Atmos. Sci.,* **35,** 561–571.

Tokioka, T., 1973: A stability study of medium-scale disturbances with inclusion of convective effects. *J. Meteor. Soc. Japan,* **51,** 1–10.

Tracton, M. S., 1973: The role of cumulus convection in the development of extratropical cyclones. *Mon. Wea. Rev.,* **101,** 573–593.

Troen, I., and L. Mahrt, 1986: A simple model of the atmospheric boundary layer: Sensitivity to surface evaporation. *Bound.-Layer Meteor.,* **37,** 129–148.

Wang, B., and A. Barcilon, 1986: Moist stability of a baroclinic zonal flow with conditionally unstable stratification. *J. Atmos. Sci.,* **43,** 705–719.

Yau, M. K., and M. Jean, 1989: Synoptic aspects and physical processes in the rapidly intensifying cyclone of 6–8 March 1986. *Atmos.–Ocean,* **27,** 59–86.